Computerized Medical Imaging and Graphics 104 (2023) 102170

Contents lists available at ScienceDirect

Computerized Medical Imaging and Graphics

journal homepage: www.elsevier.com/locate/compmedimag

A fully automatic method for vascular tortuosity feature extraction in the supra-aortic region: unraveling possibilities in stroke treatment planning

P. Canals [a,b,*], S. Balocco [c,d], O. Díaz [c], J. Li [a,b], A. García-Tornel [a,b], A. Tomasello [e], M. Olivé-Gadea [a,b], M. Ribó [a,b]

[a] Stroke Unit, Neurology, Hospital Vall d'Hebron, Barcelona, Spain
[b] Departament de Medicina, Universitat Autònoma de Barcelona, Barcelona, Spain
[c] Department of Mathematics and Computer Science, University of Barcelona, Barcelona, Spain
[d] Computer Vision Center, Bellaterra, Spain
[e] Neuroradiology, Vall d'Hebron Hospital Universitari, Barcelona, Spain

ARTICLE INFO

Keywords:
Stroke
Thrombectomy
Vascular tortuosity
Vascular feature extraction
Deep learning
Artificial intelligence

ABSTRACT

Vascular tortuosity of supra-aortic vessels is widely considered one of the main reasons for failure and delays in endovascular treatment of large vessel occlusion in patients with acute ischemic stroke. Characterization of tortuosity is a challenging task due to the lack of objective, robust and effective analysis tools. We present a fully automatic method for arterial segmentation, vessel labelling and tortuosity feature extraction applied to the supra-aortic region. A sample of 566 computed tomography angiography scans from acute ischemic stroke patients (aged 74.8 ± 12.9, 51.0% females) were used for training, validation and testing of a segmentation module based on a U-Net architecture (162 cases) and a vessel labelling module powered by a graph U-Net (566 cases). Successively, 30 cases were processed for testing of a tortuosity feature extraction module. Measurements obtained through automatic processing were compared to manual annotations from two observers for a thorough validation of the method. The proposed feature extraction method presented similar performance to the inter-rater variability observed in the measurement of 33 geometrical and morphological features of the arterial anatomy in the supra-aortic region. This system will contribute to the development of more complex models to advance the treatment of stroke by adding immediate automation, objectivity, repeatability and robustness to the vascular tortuosity characterization of patients.

1. Introduction

In the last years, mechanical thrombectomy (MT) has become the standard treatment for patients suffering from an acute ischemic stroke (AIS) caused by a large vessel occlusion (LVO) (Campbell et al., 2015; Turk et al., 2019). MT achieves rates of significant recanalization (mTICI[1] ≥ 2B: reperfusion in greater than 50% of the target cerebral ischemic territory) in 70–80% of treated patients (Flottmann et al., 2018; Yoo and Andersson, 2017). However, there is still a significant gap between angiographic results and the observed clinical outcome, where more than 50% of treated patients will not regain functional independence at 3 months (Goyal et al., 2016; Albers et al., 2018; Berkhemer et al., 2015; Jovin et al., 2015; Nogueira et al., 2018). In order to improve outcomes, it is essential to reduce interval times in all steps of the AIS treatment protocols, including not only pre- and in-hospital phases but also intraprocedural steps.

Vascular tortuosity and difficult catheter access (DCA) are two main drivers of intra-procedural time delays (Yoo and Andersson, 2017; Mont`Alverne et al., 2020; Yeo et al., 2019; Kaesmacher et al., 2018). The presence of pronounced vascular tortuosity in the aortic arch (AA) and cervical arteries can lead to failure in reaching the LVO causing the stroke with endovascular MT devices. Impossibility to reach the LVO may account for up to one third of reperfusion failures (Kaesmacher et al., 2018). Nonetheless, the overall rate of failed MTs due to unreachability of the LVO remains low, at around 4.4% (Penide et al., 2021). Time delays related to DCA during MT procedures to reach the target LVO are far more prevalent. A carotid catheterization time ≥ 30 min or a procedural time ≥ 60 min are often considered as DCA in MT

* Corresponding author at: Stroke Unit, Neurology, Hospital Vall d'Hebron, Barcelona, Spain.
E-mail address: perecanalscanals@gmail.com (P. Canals).

[1] mTICI: modified treatment in cerebral infarction.

https://doi.org/10.1016/j.compmedimag.2022.102170
Received 23 March 2022; Received in revised form 14 November 2022; Accepted 24 December 2022
Available online 28 December 2022

procedures (Mokin et al., 2020; Alawieh et al., 2019; Ribo et al., 2013; Holswilder et al., 2022), although this threshold can be even lower as suggested in (Mont`Alverne et al., 2020). About 25–30% of MTs present a difficult femoral access (Mokin et al., 2020; Ribo et al., 2013; Gomez-Paz et al., 2021), which is associated with a lower rate of recanalization and a lower rate of functional independence at 90 days (Albers et al., 2018; Ribo et al., 2013; Alawieh et al., 2019). As a result, in daily practice, the absence of solid models able to predict DCA, can lead to sequential attempts and delays through alternate access sites (i.e., femoral, radial, carotid) until the LVO is finally reached.

1.1. Recent works

The growing number of publications aiming to unravel correlation between DCA indicators and tortuosity features indicates that identifying patients with challenging anatomies pre-operatively represents an unmet need. For example, Mokin et al. (Mokin et al., 2020) (n = 100) found that angulation of the CCA and the extracranial ICA, as well as the tortuosity index of the CCA-brachiocephalic segment were significant indicators for difficult thrombectomy cases. Kaymaz et al. (Kaymaz et al., 2017) analyzed geometrical features of the supra-aortic vessels (take-off angles and tortuosity) and sought correlations with ICA access time. They found that ICA access time was significantly influenced by the left CCA (LCCA) take-off angle, brachiocephalic trunk (BT) take-off angle, and tortuosity of the CCA (n = 76). Other studies found significant correlation between MT difficulties and presence of kinks (Benson et al., 2020) or vessel curvature in 2D projections of fluoroscopic images (Schwaiger et al., 2015). An extensive comparison between tortuosity features and difficult MT indicators among these studies can be found in the supplementary material (Table S1).

Other papers focus on developing classification criteria for difficult patients with risk scores. Snelling et al. (Snelling et al., 2018) presented the B.A.D. score, an index based on the presence of a series of tortuosity-related features (AA type, presence of bovine AA, kinks, tortuosity or coiling) to determine, pre-operatively and based on visual inspection, whether a patient's vasculature is difficult or not. Ribó et al. (Ribo et al., 2013) proposed another risk score of difficult supra-aortic access based on patient's clinical data.

These studies have in common that the measurement of tortuosity-related features is at best semi-automatic (Mokin et al., 2020), while some rely on completely manual processes (Kaymaz et al., 2017; Benson et al., 2020; Schwaiger et al., 2015; Snelling et al., 2018; Rosa et al., 2021). This makes them unsuitable as acute decision-making tools in the selection of the ideal access site.

Few studies have presented automatic or semi-automatic quantitative analysis methods to address vascular segmentation and tortuosity. This is the case for Deshpande et al. (Deshpande et al., 2021), who recently presented an automated method for segmentation and feature extraction to find relevant differences regarding cerebral vasculature between stroke and healthy subjects. However, no method for vessel labeling is included, heavily limiting the characterization power of the method over individual vessels or determined vascular pathways. Moreover, the validation of the extracted feature measurements is only inferred from a thorough validation of the segmentation algorithm. Chen et al. (Chen et al., 2018) present a semi-automatic method for artery tracing, labelling and feature extraction for the cerebral arteries, validated through comparing the bifurcation placement by the algorithm against a human observer, lacking full automation of the artery tracing and labelling processes. An automatic method for labelling of the main aortic branches and landmark detection is described in (Tahoces et al., 2020), missing automatic segmentation.

Despite the remarkable achievements of these studies, there is still a lack of an automatic algorithm that includes vessel segmentation, vessel labelling and feature extraction capable of measuring vessel-specific anatomical features. All these characteristics may be necessary for effective use in clinical setting, with an emphasis on full automation of the process. This research presents a comprehensive solution to the described drawbacks while delivering comparable or better performance to the existing methods.

1.2. Contributions

This paper presents a robust, fully automated system capable of characterizing and measuring anatomical supra-aortic vascular tortuosity features using baseline computed tomography angiography (CTA). The methodologies used in each stage of the analysis pipeline are not novel individually, but the combination of such blocks in an efficient way and its clinical validation is completely innovative, and that provides a novel tool not available yet in the literature. The main contributions of this research are:

- A fully automated pipeline for the analysis of vascular tortuosity in the supra-aortic region from CTA imaging, making it possible to perform a comprehensive analysis of the vascular tortuosity within the stroke context.
- Inclusion of an integrated automatic vessel labelling method, allowing for an analysis based around the extraction of vessel-specific tortuosity features.
- Extensive validation of 33 measured features against two human observers.

The current study is part of Arterial©,[2] a vascular analysis framework created with the goal of delivering an immediate, fully automated analysis of the vascular anatomy for each stroke patient, in order to offer pre-procedural decision support for the clinician ahead of MT.

2. Methods

The proposed framework includes four modules designed to perform different tasks, implemented to analyze 3D CTA images and return a series of geometrical and morphological features automatically. These modules are, in order of sequence: vessel segmentation, vascular centerline extraction, vessel labeling and tortuosity feature extraction. A flowchart of the present study, including a simplified layout of the implemented method, is depicted in Fig. 1.

3. Dataset

We performed a retrospective analysis of a prospectively maintained database that includes all patients who underwent MT and whose basal pre-operatory imaging was acquired at Hospital Vall d'Hebron (Barcelona, Spain) between 2018 and 2021 (n = 715). Anonymized pre-procedural CTA scans from 566 patients were collected (aged 74.8 ± 12.9,[3] 51.0% females). Ethics approval was obtained from the local institutional review board [project reference: PR(AG)484/2021].

All subjects were imaged with a standard CTA image acquisition protocol using a CT system (SOMATOM Definition AS+ 128-slice, Siemens, Erlangen, Germany). Radiation dose was set to 200 mAs with a tube potential of 100 kV. Collimation was configured at 128 slices of 0.625 mm of thickness, with an increment of 0.4 mm, a rotation time of 0.5 s and a pitch of 1. A median H20s kernel from Siemens was used for the image reconstruction. Each frame was recorded in a 512 × 512 matrix with a FOV of 350 mm. Iodinated IV contrast was given in a single bolus to the patient at a rate between 4 and 5 ml/s with an overall volume of 40–80 ml of contrast solution depending on the patient. Full resolution images presented a median voxel size of 0.430 × 0.430 × 0.400 mm^3 and a median shape of 512 × 512 × 816.

[2] ©2021, copyright by VHIR and UB. All rights reserved.

[3] Standard deviation. Same convention used throughout the article unless specified otherwise.

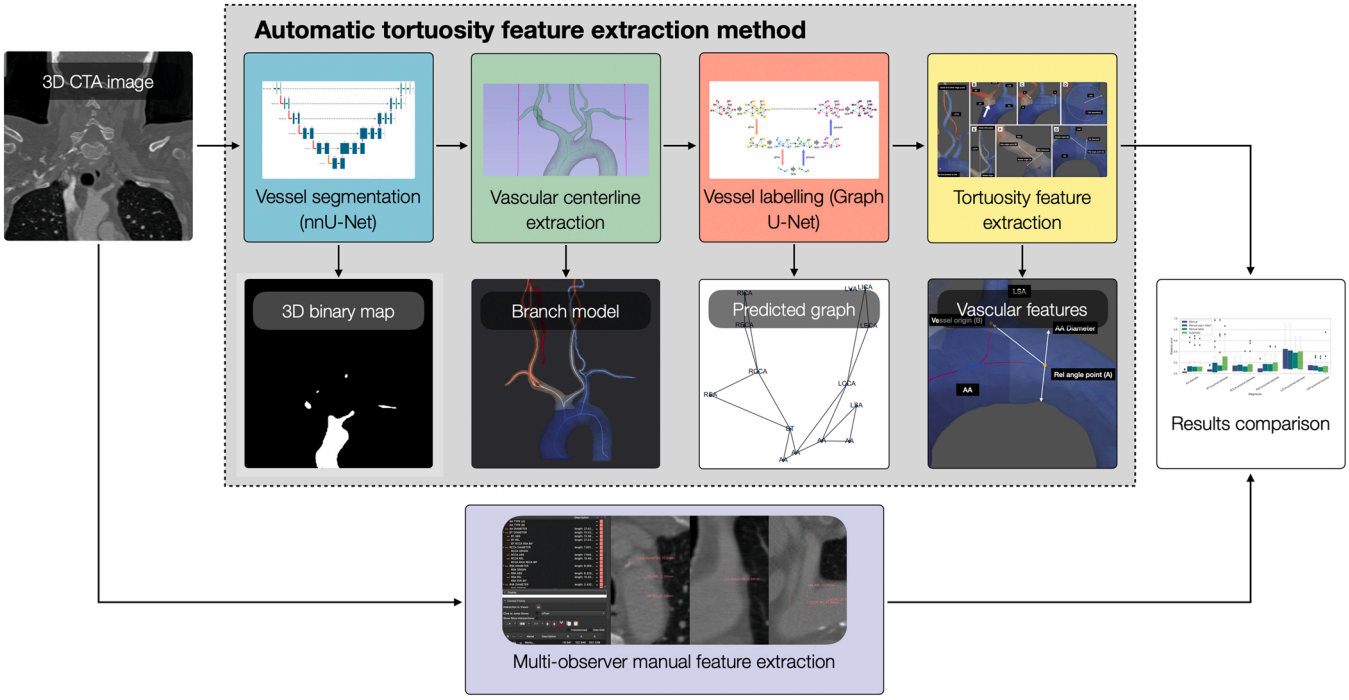

Fig. 1. Flowchart of the validation of the automatic tortuosity feature extraction method. The presented method is displayed enclosed in the grey box, with each of the four upper blocks representing the different modules of the image processing pipeline. The main output of reach of these modules is shown in the lower blocks. Results from the automatic analysis are assessed by comparing them to the ground truth obtained from averaging manual measurements from two observers.

DICOM images were converted to NIfTI and a preprocessing in the form of intensity and spatial normalization of the volumes of interest was applied prior to segmentation (Isensee et al., 2021).

From each CTA scan, a series of annotated data was generated to train, validate and test the models involved in the proposed framework. Among all available patients, 165 cases with an acute ischemic stroke secondary to a LVO, were randomly selected to form a labelled dataset for segmentation. Three cases were finally discarded due to the presence of significant imaging artifacts, leaving the final sample at 162 patients. This set was segmented once by either two engineers with + 2 years of experience (40 by engineer I and 50 cases by engineer II out of 162) or a neurologist with + 5 year of experience (72 cases out of 162) using 3D Slicer software (version 4.11) (Fedorov et al., 2012). Centerline models for the whole database (n = 569) were automatically extracted and put into graph form. Graph nodes, representing the different centerline segments, were manually annotated with the corresponding artery names by one observer (engineer I).

Table 1 displays the dataset organization for each of the modules that require testing. For segmentation, 132 cases were used for training and validation, while the remaining 30 cases (18.5% of the available images) were reserved for testing. In the 30 cases from the segmentation testing set, manual measurements were also performed by two expert observers (engineer I and the neurologist) for geometrical and morphological feature extraction assessment of the automatic and semi-automatic methods analyzed in this study, resulting in two annotation sets of 45 measurements per case. For vessel labelling, 132 manual segmentations from the segmentation training set and 377 inferred segmentations resulting from the segmentation module were used to generate centerline graphs, which following manual annotation were used for training and validation (n = 509), while 57 cases (including the 30 cases from the segmentation and feature extraction testing set) were used for testing, resulting in 10% of the overall dataset.

An analysis of the Bayes Error Rate (BER) was made for both the segmentation and the labelling modules to approximate the asymptotical performance of the model with a growing dataset. This can be used to estimate the dataset size needed to reach very close (>99%) to the asymptotical performance of the model without having to generate an infinite amount of data — a very costly process. Results for the BER that suggest the adequacy of the dataset sizes used for both modules can be found in the supplementary material (Figs. S1 and S3).

3.1. Segmentation

The first step towards automated tortuosity feature extraction for the vasculature relevant to stroke is the automatic segmentation of the arteries in the supra-aortic region from CTA volumes. nnU-Net (Isensee et al., 2021) was used as the base framework for the automatic segmentation of the volumes of interest. nnU-Net performs a thorough preprocessing of the training dataset, including spatial and intensity normalization, to automatically infer several relevant hyperparameters of the resulting 3D U-Net (Çiçek et al., 2016; Ronneberger et al., 2015). Semi-random image patching was used for data augmentation during training. The patch size as well as the batch size were automatically determined by nnU-Net, depending on the median image shape in the dataset and graphics processing unit (GPU) memory limitations. Stochastic gradient descent (SGD) with Nesterov momentum ($\mu = 0.99$) was used as the optimizer for the network, and the loss function was computed as the sum of binary cross entropy and Dice loss. Differently to the default configuration of the nnU-Net, the learning rate schedule was modified to PyTorch's ReduceLROnPlateau,[4] with an initial learning rate of 0.01, following an optimization study performed with a reduced dataset. nnU-Net applies a series of randomized operations over the selected patches for each training step for data augmentation (Isensee et al., 2021).

A five-fold cross-validation strategy was employed to assess the performance of the trained nnU-Net model, with the dataset distribution described in Table 1. The Dice coefficient (Dice, 1945), recall and the volume correlation coefficient were used as quantitative segmentation

[4] ReduceLROnPlateau I parameters: factor = 0.2, patience = 10, threshold = 0.01, mode = "min", threshold_mode = "rel".

Table 1
Organization of the data for vessel segmentation, vessel labelling and tortuosity feature extraction modules. Same 30 cases from the testing set of the segmentation module are kept for within the vessel labelling testing set and used for the feature extraction module to avoid overfitting.

	Number of annotations	Annotation type	Training	Validation	Testing
Segmentation	162	Binary map	110	22	30
Vessel labelling	566	Labeled graph	433	76	57
Feature extraction	30 (×2)	Manual measurements	-	-	30 (×2)

quality indicators. These evaluation metrics were found to be the strongest indicators for segmentation quality following an internal study involving 11 different metrics that were compared to Likert scale qualitative scores attributed to a sample of 20 cases by four different independent experts. UNETR (Hatamizadeh et al., 2022) and SwinUNETR (Tang et al., 2021) models were also implemented for our task. The most recent benchmarks show an incremental improvement of transformer models over fully convolutional networks for medical segmentation tasks (Tang et al., 2021). However, for 3D vascular segmentation tasks like hepatic vessel segmentation, nnU-Net has delivered the best results in benchmarks (Tang et al., 2021), and our experiments have also showed the superior performance of nnU-Net for our targets.

Robustness to noise was also tested by adding artificial random Gaussian noise to images increasingly to see how performance is maintained compared to baseline images. A detailed analysis can be found in the supplementary material (Fig. S2).

3.2. Centerline extraction

Fig. 2 displays the different steps of the analysis process from the input CTA up the graph generation. From the binary map obtained by segmentation (Fig. 2A-B), automatic surface model extraction is trivially performed by thresholding (Fig. 2 C), followed by smoothing and removal of small islands. Intracranial arteries are ignored for the rest of the analysis.

Centerline models are then extracted via shortest path tracing between automatically detected extremal points (startpoint and endpoints), placed at the end of vascular structures. Paths are defined over the Voronoi diagram corresponding to the closed surfaces resulting from the binary map segmentation. Shortest paths between the startpoint and the endpoints are determined by minimization of a wave propagation integral described by the Eikonal equation (Antiga et al., 2003) (Fig. 2D). For centerline and surface model branching, tubes are conformed for each centerline segment by joining the maximal inscribed spheres associated to each centerline point. Tube containment relationships between centerlines and tubes are defined following reference point placement (intersections between centerlines and tubes), which enable branch splitting for both the centerline and surface models (Antiga and David, 2004) (Fig. 2E). The described methods for centerline extraction and branch splitting are implemented in the Vascular Modelling Toolkit (VMTK, version 1.4) (Antiga et al., 2008), used here for these computations. Custom modules were designed and added to the VMTK methods for a robust endpoint auto-detection and for circular centerline tracing.

The resulting branched centerline model is used to generate a graph, where nodes correspond to centerlines of individual vascular segments, which are connected by edges to the immediately proximal and distal segments in contact (Fig. 2 F).

3.3. Vessel labeling

A graph U-Net (gU-Net) (Gao and Ji, 2019) model was used for vessel labelling of the centerline models. Graph nodes were characterized with node attributes obtained from the centerline models. A total of 24 node attributes were computed, including the mean, proximal, distal, maximum and minimum radius, proximal/distal radius ratio, Euclidean distance between proximal and distal bifurcation points, relative length (RL) of the segment, overall direction, departure direction (given by the vector joining the first two points of the segment), number of points of the centerline segment, proximal and distal bifurcation positions and center of mass. Data augmentation is applied in the form of increased connectivity of the nodes by edge linking to all those nodes within 10 mm (found empirically) of the node's center of mass, and normalization of all attribute to their mean value averaged across the training set. Proximal/distal radius ratio and RL are not normalized since these are already relative measurements, and direction 3D vectors are normalized to unitary vectors.

An optimization study, including 288 different variations for the gU-Net architecture and training configuration, was performed to identify the best combination of hyperparameters for the model. The model with the best testing accuracy was selected. The network's architecture is characterized by four pooling steps (depth = 3), with pooling ratios of 0.5 each, and with graph convolution network (GCN) layers at each level. Skip connections connect the equivalent levels from the encoder and decoder blocks. The number of hidden channels for the node embeddings was set to 64, while the batch size was set to 20.

SGD with high momentum ($\mu = 0.99$) and a weight decay of 10^{-3} for regularization was used as optimizer, with an initial learning rate of 10^{-2}, scheduled with ReduceLROnPlateau.[5] The cross entropy was used as the loss criterion for node classification. Early stopping was employed to prevent overfitting, with validation loss serving as the early stopping criteria. The data organization for training, validation and testing is described in Table 1. Five-fold cross-validation was used to ensure the validity of results. Edge accuracy per case, computed as the percentage of correct predictions over the total sample, overall accuracy (pooling all predictions), overall Dice coefficient, recall, precision, class-wise Dice coefficient and error occurrences per case were used to assess the gU-Net's performance.

3.4. Tortuosity feature extraction

3.4.1. Manual feature extraction

To validate the automatically extracted tortuosity features, the feature extraction testing set (n = 30) was manually processed by two different expert observers where a total of 45 different geometric and morphological features were extracted directly from raw CTAs. Morphological features include presence of a bovine AA (Layton et al., 2006), presence of aberrant right subclavian artery (ARSA) (Chaoui, Rake, and Heling, 2008) and AA type (Bajzer, 2004). Geometrical features include proximal diameter, RL (Kliś et al., 2019), and absolute and relative polar and azimuth departure angles. Geometrical features are extracted for the brachiocephalic trunk (BT), right common carotid artery (RCCA), right subclavian artery (RSA), right vertebral artery (RVA), left common carotid artery (LCCA), left subclavian artery (LSA) and left vertebral artery (LVA). In addition, the diameter at the apex was also measured for the AA. The presence of ARSA was finally excluded as none of the patients from the testing set presented it.

3.4.2. Automatic feature extraction

The same fundamental criteria (landmark localization) were adopted

[5] ReduceLROnPlateau II parameters: factor = 0.5, patience = 20, threshold = 0.01, mode = "min", threshold_mode = "rel".

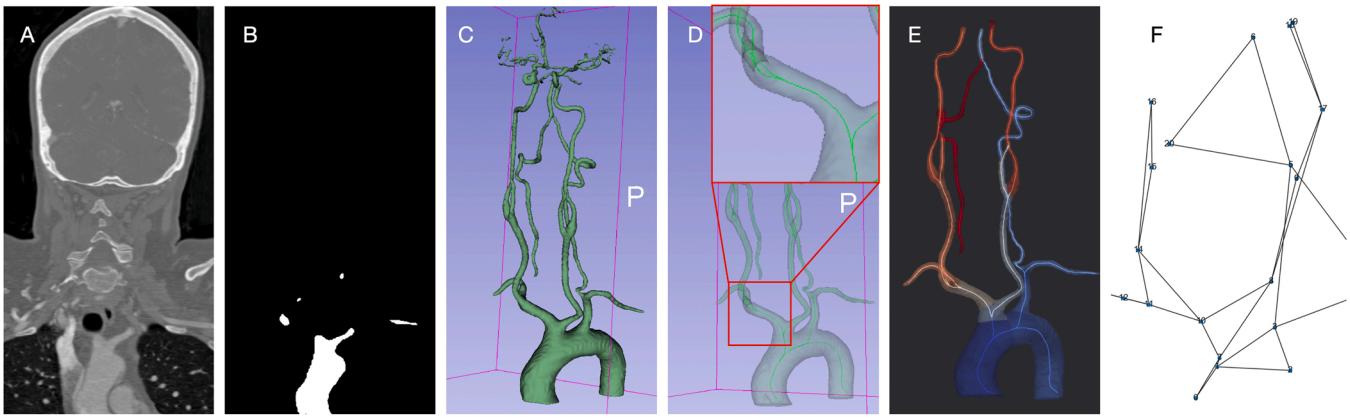

Fig. 2. Data processing from the CTA images, through centerline extraction and branching, up to graph generation. (A) Original CTA volume. (B) Binary map output by the segmentation module. (C) Volume model from binary map. (D) Volume model with extracted centerline model. (E) Branched centerline model over clipped surface model output by the centerline extraction module. (F) Graph corresponding to the centerline mesh.

for the automatic feature extraction method. All centerline branches with the same predicted type (i.e., vessel name) following automatic labelling were joint as a single vascular segment. VMTK variables from the branched centerline model and the clipped surface model were used to locate relevant landmarks (e.g., vessel origin, proximal and distal ends, absolute angle point, AA type landmarks). The centerline model was used to compute the diameter at any point, using the maximal inscribed sphere radius. *A priori* knowledge (mainly, known connection relationships between arteries) was used to locate the relative angle point and recognize bovine AA and ARSA presence. Fig. 3 shows a series of example sketches for most of the measurements performed for the automatic feature extraction process.

Vertebral artery (VA) tortuosity features were discarded from the analysis due to a high number of cases with missed automatic segmentations at the base of the VAs from the corresponding subclavian artery (SA) bifurcation, which resulted in a high percentage of missed measurements. Imaging artifacts were often found to be responsible for a sub-optimal imaging at the VA origin in a large fraction of cases, resulting in underperforming segmentation at these locations. This left a final group of 33 tortuosity features left for analysis.

3.5. Statistical analysis

Inter-observer variability was assessed and used as a reference measure. Averaged measurements between observers were used as ground truth values. The performance of the automatic method was assessed differently for morphological and geometrical tortuosity features. As categorical variables, morphological features were evaluated using the Cohen's kappa (κ) (Cohen, 1960) in the case of the bovine AA presence, and the linearly weighted Cohen's kappa (κ_L) for the AA type. For geometrical tortuosity features, the two-way mixed effects, single rater intra-class correlation coefficient (ICC) for absolute agreement (Koo and Mae, 2016) was used to assess the reliability across human observers and the automatic method. ICC thresholds of 0.5, 0.75 and 0.9 were used to assess the agreement across methods as poor (ICC $<$ 0.5), moderate (0.5 $<$ ICC $<$ 0.75), good (0.75 $<$ ICC $<$ 0.9) or excellent (ICC $>$ 0.9).

Bland-Altman plots (Martin Bland and Altman, 1986) were also drawn for all features and are available in the supplementary material (Figs. S5-S10). Bias and 95% CI values of the error distribution were computed for both methods as a complementary performance measure, and box plots for the absolute error (and relative error in the case of diameter measurements) were drawn for error distribution visualization.

For inter-observer reliability assessment, values from both observers were compared to each other to avoid influence of co-dependency with ground truth values. For the automatic method, values were compared to the ground truth.

Landmark placement was also quantitatively evaluated. Precision, recall and mean distance error were used to compare the presented method for landmark localization to other state-of-the-art algorithms proposed in the literature. For precision and recall computation, true positives (TPs) were recorded as landmarks placed at a distance error smaller than a given threshold, while false positives (FPs) were landmarks placed outside of the local region defined by this cut-off. This threshold was taken as the proximal diameter of the vessel associated to each tortuosity feature, averaged across all cases (e.g., for the BT origin, the average BT proximal diameter was used as threshold). False negatives (FNs) are defined as measurements that were manually recorded, but were missed by the algorithms.

4. Results

4.1. Segmentation

The nnU-Net was the best performing model out of those tested. A mean Dice coefficient of 0.93 $\pm$ 0.02 and a recall of 0.93 $\pm$ 0.03 were obtained in testing over the five folds. The mean volume correlation coefficient was 0.998 $\pm$ 0.003. Table 2 shows a comparison between the present and other state-of-the-art 3D vessel segmentation algorithms applied on similar segmentation targets.

Qualitatively, satisfactory performance of the segmentation process for the AA region, common carotid arteries (CCAs) and subclavian arteries (SAs) (Fig. 4 A) was observed. However, VAs tended to present segmentation errors at the origin, as well as discontinuities along the vessel (Fig. 4B). Cerebral arteries were accurately segmented up to the circle of Willis (Fig. 4 C). Distal SAs and external carotid arteries (ECAs) were generally not entirely segmented, as training data did not include these in most manual annotations.

Regarding architectural details of the model, the number of downsampling operations was determined upon choice of the patch size for forward processing. For the used dataset, a patch size of 112 $\times$ 112 $\times$ 192 was selected after dataset preprocessing following limitations of both GPU memory and mathematical restrictions due to needed downsampling operations, as per nnU-Net design rules (Isensee et al., 2021). Thus, the network had 6 spatial resolution levels derived from 4 downsampling steps for the coronal and sagittal directions and an additional one for the axial direction. Encoder steps were constructed with a 3D convolutional kernel of size 3 $\times$ 3 $\times$ 3, followed by instance normalization (IN) and a leaky ReLU activation function. Downsampling was applied by strided 3D convolution (stride = 2), with kernel size of 2 $\times$ 2 $\times$ 2, doubling the number of channels at each step. In the decoder

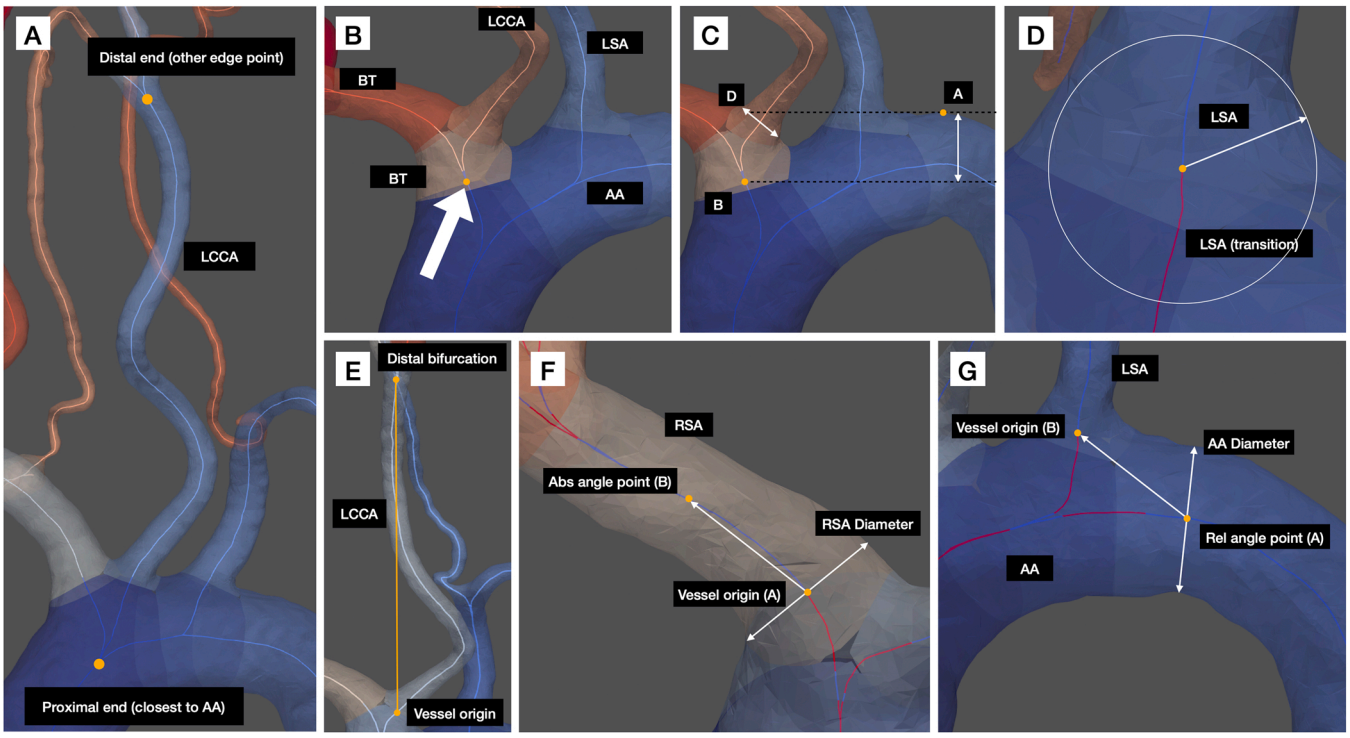

Fig. 3. Sample of automatically extracted features. (A) Oriented vascular segment for the LCCA. (B) Bifurcation between the LCCA and BT in a bovine AA. (C) Points A and B, and LCCA diameter D used for the AA type computation. (D) Proximal diameter measured at the LSA origin. The white circle represents the maximal inscribed sphere radius, projected in 2D. (E) Scheme of the RL computation for a LCCA. (F) Scheme of the absolute angle point placement for a RSA. (G) Scheme of the relative angle point placement for an LSA, with the preceding vessel being the AA.

block, 3D transpose convolution kernels of shape $2 \times 2 \times 2$ were employed for upsampling, and two convolutional kernels of $3 \times 3 \times 3$ (with IN and leaky ReLU) are applied, halving the number of channels at each level. Skip connections were used to concatenate feature maps from encoder and decoder blocks. Convolutions of $1 \times 1 \times 1$ followed by softmax layers were used to determine final activation of the decoder block at each of the resolution levels (except the two lowest resolutions), and deep supervision was used for loss computation during training. For inference, segmentation prediction was derived from the softmax activation of the final decoder step.

An experiment to test robustness to noise was also performed. Results shows how the implemented segmentation model is able to maintain performance with noise levels up to 5 times higher than the typical noise levels on CT (Fig. S2).

4.2. Vessel labeling

Table 3 compares the performance of the presented method to other state-of-the-art studies with similar labelling objectives. An edge prediction accuracy per case of 0.95 ± 0.06 resulted from the gU-Net trainings across folds. Table 4 shows the class-wise Dice coefficient for each of the edge classes available for vessel labelling by the gU-Net. Frequent errors (mistakes repeated four or more times within the testing set, $n = 57$ cases) include wrong prediction of right external carotid artery (RECA) for right internal carotid artery (RICA) (5 times) and AA for BT segments (4). Regarding error occurrences, 1.1 labelling errors per graph were made on average over the testing set, with 16.8 nodes per case, 42.1% of cases presented perfect labelling (70.2% presented one error or less).

4.3. Tortuosity feature extraction

Table 5 shows a comprehensive evaluation of the acquisition methods performance for each tortuosity feature.

Table 2
Comparison between the segmentation performance (Dice coefficient) of the used method (nnU-Net) and other state-of-the-art methods with similar segmentation targets. Black font highlights best metric (same convention used in other tables within the present study).

	Model	Image modality	Imaged anatomy	N	Dice
Ours (2022)	nnU-Net	CTA	Head + neck + AA	162	0.93 ± 0.02
Ours (2022)	SwinUNETR	CTA	Head + neck + AA	162	0.88 ± 0.05
Ours (2022)	UNETR	CTA	Head + neck + AA	162	0.74 ± 0.10
Fu et al. (2020)(Fu et al., 2020)	ResU-Net	CTA	Head + neck + AA	18,259	**0.95**
Fantazzini et al. (2020)(Fantazzini et al., 2020)	2D U-Nets	CTA	Aorta	80	0.92 ± 0.01
Fan et al. (2020)(Fan et al., 2020)	HMRF + U-Net	TOF MRA	Cerebral arteries	100	0.79 ± 0.05
ElHadji et al. (2019)(Hadji et al., 2019)	ResU-Net	CE-CBCT	Cerebral arteries	25	0.79 ± 0.13
Livne et al. (2019)(Livne et al., 2019)	Half U-Net	TOF MRA	Cerebral arteries	66	0.92
Phellan et al. (2017)(Phellan et al., 2017)	Deep CNN	TOF MRA	Cerebral arteries	4	0.77 ± 0.01
Isensee et al. (2021)(Isensee et al., 2021)	nnU-Net	CTA	Hepatic vessels	443	0.69

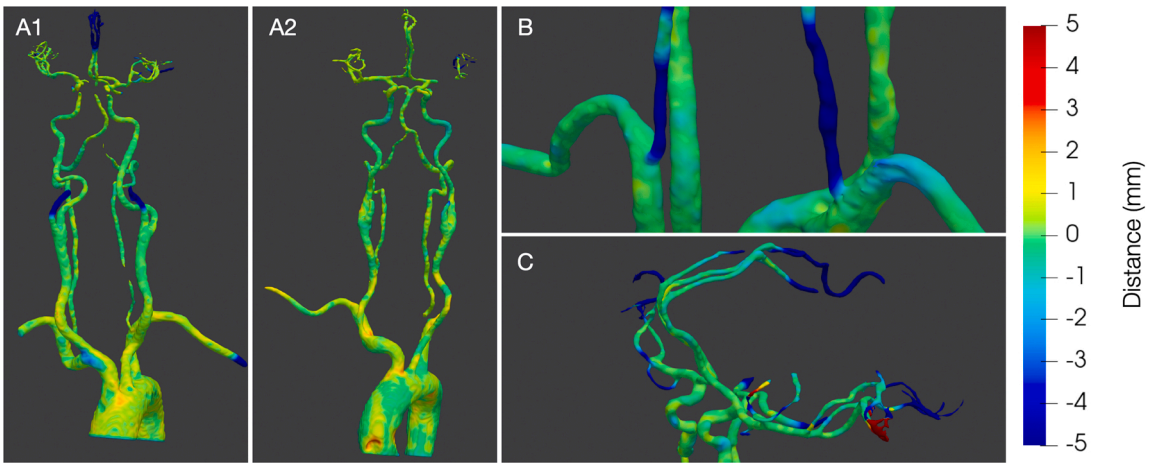

Fig. 4. error distance maps between the predicted segmentations obtained from the automatic segmentation through the nnU-Net, and the manual segmentations. (A) Distance maps for the whole segmentation target, showing good behavior in the supra-aortic region. (B) Missed segmentations at the base of the VAs. (C) Distal cerebral arteries are not accurately segmented in a significant number of cases. Positive distances represent over-segmented regions, while negative distances highlight under-segmentations.

4.3.1. Manual feature extraction

Inter-observer variability is assessed in this section as a reference measure. Only three geometrical features presented poor reliability across both human observers. Fourteen features presented excellent agreement while 12 presented good agreement, leaving 2 with moderate reliability. Regarding morphological features, there was perfect agreement on bovine AA presence, and moderate agreement was found for the AA type measurement across observers.

Reliability across observers was weaker for diameter measurements (4 out of 6 features presented weak to moderate agreement), good to excellent for angle measurements and excellent for all RL measurements.

4.3.2. Automatic feature extraction

The automatic method presented comparable performance to the manual feature acquisition. Only three features presented poor reliability compared to the ground truth values. Ten features presented excellent agreement, while 9 showed good reliability. The remaining 9 features had moderate agreement with reference values. For morphological features, performance of the automatic method was equivalent to human performance.

Missed segmentations and inaccurate vessel labelling can make some measurements impossible to perform in automatic feature extraction, as some landmarks are not located. However, the number of missed landmarks was low, only a 2.6% of the total number of landmarks across all cases, yielding a total of 3.3% missed measurements across the complete sample. These values were omitted for the computation of the ICC and error distributions.

Fig. 5 shows a visual representation of the error distribution for each geometrical feature and method. The proposed method presented very similar error distributions compared to the inter-observer variability found for most features, with a slightly higher median value and broader interquartile ranges across the feature set.

Table 6 shows precision, recall and mean error for the landmark placement, comparing the manual and proposed methods against other state-of-the-art algorithms with similar landmark localization targets in vascular anatomies. The error distribution across methods for the landmark placement can be found in the supplementary material (Fig. S4).

5. Discussion

To our knowledge, this is the first research introducing a fully automatic pipeline for the characterization of vascular tortuosity in the supra-aortic region. We implemented, adapted and combined several

Table 4
Number of vessels (N), TPs, FPs, FNs and Dice coefficient for each of the possible vessel types present in the node classification by the gU-Net, over predictions with the testing set. BA: basilar artery.

Vessel type	N	TP	FP	FN	Dice
Other	30	23	5	7	0.79
AA	226	225	9	1	0.98
BT	57	52	1	5	0.95
RCCA	56	54	0	2	0.98
LCCA	60	56	1	4	0.96
RSA	95	91	4	4	0.96
LSA	100	94	6	6	0.94
RVA	50	44	8	6	0.86
LVA	57	51	9	6	0.87
RICA	51	44	3	6	0.91
LICA	50	44	3	6	0.91
RECA	53	51	8	2	0.91
LECA	56	52	4	4	0.93
BA	15	13	2	2	0.87
Total	956	894	62	62	0.94

Table 3
Overall vessel prediction accuracy, precision, recall and Dice coefficient for the presented gU-Net and other state-of-the-art methodologies proposed for similar labelling tasks. *Method from (Chen et al., 2020) was implemented and tested with our data.

	Method	Target	Accuracy	Precision	Recall	Dice
Ours (2022)	Graph U-Net	Head + neck + AA	**0.94**	0.94	**0.94**	**0.94**
Yao et al. (2020) (Yao et al., 2020)	GCN-point cloud	Head + neck + AA	0.93	-	-	0.92
Chen et al. (2020)(Chen et al., 2020)	GNN	Cerebral arteries	0.92	-	-	-
Chen et al. (2020) *	GNN	Head + neck + AA	0.82	0.84	0.83	0.83
Dunås et al. (2016)(Dunås et al., 2016)	ATLAS	Cerebral arteries	0.93	-	-	-
Tahoces et al. (2020)(Tahoces et al., 2020)	*A priori* knowledge	Aorta branches	-	**0.99**	0.92	-

Table 5
Performance of the acquisition methods for all analyzed features. ICC, bias and 95\% CI of the error distribution for the inter-observer variability (manual) and the automatic method are displayed for geometrical features. Those features with poor agreement are highlighted in red. Below, κ and κL values for the bovine AA presence and the AA type are exhibited, respectively.

Geometrical feature	ICC		Bias (error 95% CI)		
	Manual	Automatic	Manual	Automatic	Units
AA diameter	0.89	0.78	-1.04 (2.57)	1.00 (3.41)	mm
BT proximal diameter	0.70	0.67	-0.73 (3.57)	-0.44 (5.31)	mm
RCCA proximal diameter	0.37	0.59	-0.21 (3.13)	-0.32 (2.03)	mm
RSA proximal diameter	0.40	0.62	-0.28 (3.67)	1.00 (2.47)	mm
LCCA proximal diameter	0.53	0.27	-1.31 (3.11)	-0.25 (5.60)	mm
LSA proximal diameter	0.48	0.76	-1.85 (3.38)	-0.03 (1.96)	mm
BT relative length	0.99	0.89	< 0.01 (0.03)	0.01 (0.07)	-
RCCA relative length	> 0.99	0.58	< 0.01 (0.01)	0.08 (0.32)	-
RSA relative length	> 0.99	0.51	< 0.01 (0.02)	0.02 (0.23)	-
LCCA relative length	> 0.99	0.98	< 0.01 (0.01)	< 0.01 (0.04)	-
LSA relative length	> 0.99	0.54	0.01 (0.02)	0.02 (0.28)	-
BT abs polar angle	0.81	0.87	-0.07 (0.31)	-0.06 (0.42)	rad
BT abs azimuth angle	0.91	0.83	0.05 (0.58)	-0.35 (1.61)	rad
BT rel polar angle	0.86	0.87	0.16 (0.24)	0.15 (0.37)	rad
BT rel azimuth angle	0.85	0.83	-0.04 (0.15)	-0.06 (0.28)	rad
RCCA abs polar angle	0.83	0.53	-0.02 (0.39)	-0.03 (0.61)	rad
RCCA abs azimuth angle	0.85	0.71	-0.04 (0.32)	-0.01 (1.00)	rad
RCCA rel polar angle	0.96	0.92	0.05 (0.22)	0.01 (0.33)	rad
RCCA rel azimuth angle	0.88	0.94	0.05 (0.34)	0.04 (0.61)	rad
RSA abs polar angle	0.79	0.82	0.07 (0.58)	0.02 (0.51)	rad
RSA abs azimuth angle	0.98	0.43	-0.04 (0.31)	-0.14 (1.12)	rad
RSA rel polar angle	0.93	0.96	-0.04 (0.32)	-0.10 (0.21)	rad
RSA rel azimuth angle	0.87	0.84	-0.09 (0.30)	-0.10 (0.96)	rad
LCCA abs polar angle	0.91	0.76	< 0.01 (0.19)	-0.08 (0.31)	rad
LCCA abs azimuth angle	0.99	0.94	0.03 (0.23)	0.10 (1.40)	rad
LCCA rel polar angle	0.84	0.15	0.11 (0.26)	0.09 (0.66)	rad
LCCA rel azimuth angle	0.97	0.94	0.01 (0.10)	-0.08 (0.32)	rad
LSA abs polar angle	0.94	0.93	< 0.01 (0.15)	-0.08 (0.15)	rad
		333			
LSA abs azimuth angle	0.98	0.98	-0.01 (0.35)	0.07 (0.69)	rad
LSA rel polar angle	0.87	0.94	0.14 (0.20)	0.03 (0.13)	rad
LSA rel azimuth angle	0.83	0.90	< 0.01 (0.12)	-0.03 (0.18)	rad
Morphological feature	Automatic				
Bovine AA presence (κ_L)	1.00				
AA type (κ)	0.52				

state-of-the-art solutions to develop a robust method for the characterization of vascular tortuosity. Compared to similar previously published studies, this research includes several key aspects such as full automation of the entire analysis pipeline, inclusion of multiple human observers for the manual acquisition of feature measurements or the inclusion of vessel-specific features.

As an objective and fast feature extraction method, automatic tortuosity characterization of patients can provide a basis for the development of predictive AI models that could confer valuable information to the clinician pre-operatively about the difficulties they might experience when navigating through the AA and the supra-aortic region. This immediate characterization system is the necessary first step in the development of a decision support tool able to guide neuro-interventionalists in their procedural planning. As a result, the initial approaches in MT procedures could be efficiently programmed, reducing access failures and workflow times, and ultimately improving clinical outcomes.

Full automation has several key advantages over semi-automatic and manual methods. Firstly, it allows the measurements process to be rapidly performed in a small amount of time. We performed the full analysis with the automatic method with all cases from the feature extraction testing set (n = 30), and measured an average computation time of 4 min 49 s ± 0 min 53 s[6] across cases. Several factors may influence the computation time such as the input image size, the number of separate segments after segmentation or the thermal throttling of the hardware components. Manual segmentation in CTA volumes of the arteries relevant for MT can typically take between 20 and 60 min per case depending on the patient, the observer's experience and the required segmentation quality. Manual vessel labelling, in comparison, is a relatively quick process, taking approximately 1–5 min per case if made by an experienced user. The manual feature extraction process is also quite intricate, taking between 45 and 60 min per case. A comparison between the time needed for each step of the process across methods is found in Table 7. The advantage of the automatic method in this regard is clear and represents the main argument for the use of the presented method, as the manual alternative is simply not feasible in the stroke treatment context due to the time needed to perform the analysis.

Secondly, bypassing any human interaction provides objectivity, repeatability and robustness to the measurement acquisition, all of which are considered key aspects for ensuring a valid characterization for each patient, independently of the rater. The third main advantage is that no specialized or trained personnel is needed to perform the analysis, which is a crucial factor for its applicability in clinical practice over any semi-automatic method.

The error distribution for most features is very similar between the manual and the automatic methods, with the addition of a few occasional outliers in the automatic case (Fig. 5, Figs. S5-S10). Generally, the automatic analysis yields accurate results for most cases in the testing set but, on occasion, some landmarks are placed far from the ground truth values causing the presence of outliers. These outliers are non-existent in manual acquisition across different observers, as virtually all landmarks were located by both observers within a reasonable distance. This makes the analysis very demanding for the automatic methodology, as the

[6] Time measurements for image processing with the automatic method were performed in a Linux server with an Intel® Xeon™ W-2275 CPU, 128 GB of RAM, and Nvidia RTX A5000 GPU (24 GB).

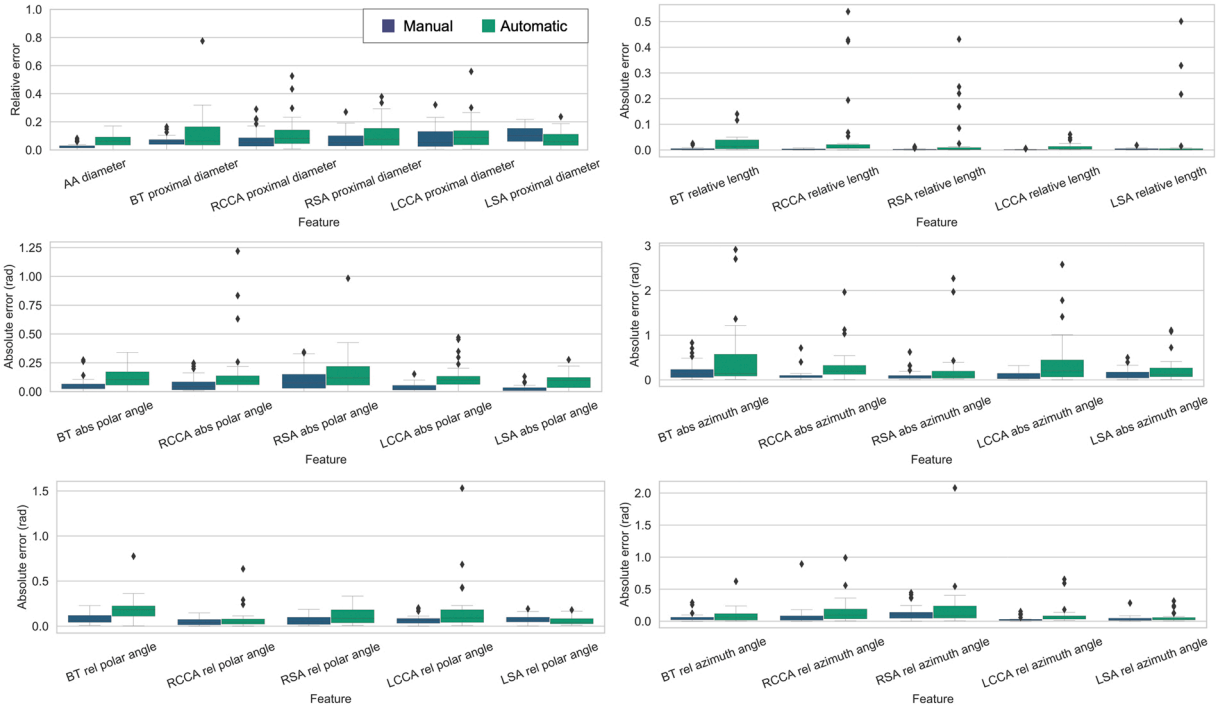

Fig. 5. Box plots of the relative error for diameter measurements and absolute error for RLs, absolute angles and relative angles, for error comparison for both methods.

Table 6
Precision, recall and mean error for the landmark placement of the analyzed methods compared to other state-of-the-art methodologies. Italic font indicates non-algorithmic acquisition methods.

	Target	Precision	Recall	Mean error (mm)
Manual	Head + neck + AA landmarks	*0.98*	*1.00*	2.9 ± 2.1
Ours (2022)	Head + neck + AA landmarks	0.81	**0.97**	2.7 ± 2.2
Chen et al. (2018) (Chen et al., 2018)	Intra-cranial arteries bifurcations	**0.94**	0.85	**0.3 ± 0.4**
Tahoces et al. (2020) (Tahoces et al., 2020)	Aorta landmarks	-	-	5.7 ± 7.3

presence of only a small number of outliers heavily influences ICC measurement and the error distribution values.

Table 2, Table 3 and Table 6 compare the obtained results for each of the presented modules with other published methods applied on similar tasks. In all three cases, state-of-the-art results are achieved with our methods, demonstrating the performance of each of the modules individually.

The error sources in the measurement of tortuosity features are diverse, due to the high number of automated operations present in the pipeline. These were identified and classified into the following categories (ordered by decreasing relevance): incorrect vessel labelling, sub-optimal segmentation, incorrect centerline extraction, incorrect data processing, unreliable azimuth angle due to steep polar component, imaging artifacts and reasonable landmark displacements.

Table 7
time comparison between manual and automatic acquisition for the time needed to perform each stage of the image processing. *Sensitive to the chosen resolution.

Process	Manual (approximation)	Automatic
Segmentation (nnU-Net inference)	40 min	2 min 3 s
Centerline extraction	5 min	1 min 17 s
Branch and clipped model computation	-	1 min 18 s*
Graph generation	-	< 1 s
Vessel labelling (gU-Net inference)	1 min	< 1 s
Feature extraction	45 min	9 s
Total	91 min	4 min 49 s

Future work within the Arterial© framework will explore predictive tasks relative to stroke patients and MT procedures, that will rely on the measurements obtained with the presented tortuosity feature extraction method. The accuracy delivered by these predictive models will ultimately determine if the performance of the tool in vessel anatomy characterization is sufficient to design efficient predictive algorithms.

One important limitation of this study is the inclusion of features that could be validated against human measurements. That significantly limits the number and the type of features that could be included in this validation assessment compared to the true potential of the presented method. Features such as mean diameter, waviness of the vessel (Hathout and Huy, 2012) or vessel volume are some examples of features that could be easily extracted by the algorithm in its current version but could not be directly validated against human measurements. In addition, tortuosity descriptors can be gathered in different scales. In this research, we have mainly looked at segment-scale features (e.g., RL, departure angles, or proximal diameters) and global features (e.g., presence of bovine AA, AA type). Features at a more local scale (e.g., curvature at any point of the centerline, diameter at any point) may also be relevant and contain valuable information to describe vascular tortuosity. Our framework offers the flexibility needed to encode all this information.

Another limitation for the current methodology is that it is limited to CTA imaging. However, since the only point of contact of the analysis

process with the input imaging is the segmentation model, this limitation could be resolved by adapting the segmentation module to other imaging sources. Such segmentation model could be trained using other kinds of imaging modalities (e.g., MRA, 3DRA, etc.) so that the analysis could be performed regardless of the input data form. The use of data originated from a single medical center and CT manufacturer are other limitations of this study.

6. Conclusion

We present a thorough validation study of a fully automatic method for segmentation, vessel labelling and feature extraction for vascular tortuosity analysis. Thirty-three geometric and morphological characteristics of the arteries in the supra-aortic region that are relevant to MT procedures were extracted by an automatic model, and results were compared to manual measurements acquired by two independent expert observers. Performance of the proposed methodology was comparable to human performance, with the advantage of a significant time reduction needed for the analysis, making it compatible with the stroke setting for pre-operatory patient assessment.

Ethics approval statement

The use of data for the submitted article was reviewed and approved by the Ethics Committee of Clinical Investigation (Comité Ètic d'Investigació Clínica, CEIC), the institutional review board of Hospital Universitari Vall d'Hebron (Barcelona, Spain), with review number PR (AG)484/2021.

CRediT authorship contribution statement

Pere Canals: Investigation, Data curation, Formal analysis, Methodology, Software, Visualization, Funding acquisition, Writing – original draft, Writing – review & editing. **Simone Balocco:** Methodology, Validation, Supervision, Writing – review & editing. **Oliver Díaz:** Methodology, Validation, Supervision, Writing – review & editing. **Jiahui Li:** Data curation. **Álvaro García-Tornel:** Data curation, Writing – review & editing. **Alejandro Tomasello:** Resources. **Marta Olivé - Gadea:** Funding acquisition. **Marc Ribo:** Conceptualization, Validation, Resources, Writing – review & editing, Project administration, Funding acquisition.

Declaration of Competing Interest

The authors declare the following financial interests/personal relationships which may be considered as potential competing interests. Pere Canals reports financial support was provided by Government of Catalonia Catalan Health Service. Marta Oliver-Gadea reports financial support was provided by Spain Ministry of Science and Innovation. Simone Balocco reports financial support was provided by Spain Ministry of Science and Innovation. Pere Canals has patent #2109279362548 issued to Vall d'Hebron Institut de Recerca (VHIR); Universitat de Barcelona (UB). Simone Balocco has patent #2109279362548 issued to Vall d'Hebron Institut de Recerca (VHIR); Universitat de Barcelona (UB). Oliver Diaz has patent #2109279362548 issued to Vall d'Hebron Institut de Recerca (VHIR); Universitat de Barcelona (UB). Marc Ribo has patent #2109279362548 pending to Vall d'Hebron Institut de Recerca (VHIR); Universitat de Barcelona (UB).

Data Availability

The authors do not have permission to share data.

Acknowledgements

This work was partially supported by the Catalan Health Department (Departament de Salut, Generalitat de Catalunya) with a pre-doctoral scholarship (PERIS PIF-Salut 2021, grant number SLT017/20/000180), the Spanish Health Institute Carlos III (Instituto de Salud Carlos III, Ministerio de Ciencia e Innovación, Gobierno de España) with a PI21 grant (PI21/01967) and grants RTI2018–095232-B-C21 and 2017 SGR 1742.

Appendix A. Supporting information

Supplementary data associated with this article can be found in the online version at doi:10.1016/j.compmedimag.2022.102170.

References

Alawieh, Ali, Jan Vargas, Kyle, Fargen, M., Farris Langley, E., Robert, M., Starke, Reade De. Leacy, Rano Chatterjee, et al., 2019. Impact of procedure time on outcomes of thrombectomy for stroke. J. Am. Coll. Cardiol. 73 (8), 879–890. https://doi.org/10.1016/j.jacc.2018.11.052.

Albers, Gregory W., Michael, P.Marks, Kemp, Stephanie, Christensen, Soren, Tsai, Jenny P., Ortega-Gutierrez, Santiago, McTaggart, Ryan A., et al., 2018. Thrombectomy for Stroke at 6 to 16 hours with selection by perfusion imaging. N. Engl. J. Med. 378 (8), 708–718. https://doi.org/10.1056/nejmoa1713973.

Antiga, Luca, David, A.Steinman, 2004. Robust and objective decomposition and mapping of bifurcating vessels. IEEE Trans. Med. Imaging 23 (6), 704–713. https://doi.org/10.1109/TMI.2004.826946.

Antiga, Luca, Bogdan Ene-Iordache, Andrea, Remuzzi, 2003. Centerline computation and geometric analysis of branching tubular surfaces with application to blood vessel modeling. Wscg. http://citeseerx.ist.psu.edu/viewdoc/download?doi=10.1.1.14.671&rep=rep1&type=pdf.

Antiga, Luca, Marina Piccinelli, Lorenzo Botti, Bogdan Ene-Iordache, Andrea Remuzzi, David, A.Steinman, 2008. An image-based modeling framework for patient-specific computational hemodynamics. Med. Biol. Eng. Comput. 46 (11), 1097–1112. https://doi.org/10.1007/s11517-008-0420-1.

Bajzer, C.T., 2004. Thoracic Aorta and the Great Vessels. In *Guide to Peripheral and Cerebrovascular Intervention*. Remedica, London. https://www.ncbi.nlm.nih.gov/books/NBK27419/.

Benson, John, Waleed Brinjikji, C., Steven, A., Messina, Giuseppe Lanzino, David, F. Kallmes, 2020. Cervical internal carotid artery tortuosity: a morphologic analysis of patients with acute ischemic stroke. Interv. Neuroradiol. 26 (2), 216–221. https://doi.org/10.1177/1591019919891295.

Berkhemer, Olvert A., Puck, S.S.Fransen, Beumer, Debbie, van den Berg, Lucie A., Lingsma, Hester F., Yoo, Albert J., Schonewille, Wouter J., et al., 2015. A randomized trial of intraarterial treatment for acute ischemic stroke. N. Engl. J. Med. 372 (1), 11–20. https://doi.org/10.1056/nejmoa1411587.

Campbell, Bruce C.V., Geoffrey, A.Donnan, Lees, Kennedy R., Hacke, Werner, Khatri, Pooja, Hill, Michael D., Goyal, Mayank, et al., 2015. Endovascular stent thrombectomy: the new standard of care for large vessel ischaemic stroke. Lancet Neurol. 14 (8), 846–854. https://doi.org/10.1016/S1474-4422(15)00140-4.

Chaoui, R., Rake, A., Heling, K.S., 2008. Aortic arch with four vessels: aberrant right subclavian artery. Ultrasound Obstet. Gynecol. 31 (1), 115–117. https://doi.org/10.1002/uog.5240.

Chen, Li, Mossa-Basha, Mahmud, Balu, Niranjan, Canton, Gador, Sun, Jie, Pimentel, Kristi, Hatsukami, Thomas S., Jenq Neng Hwang, Yuan, Chun, 2018. Development of a quantitative intracranial vascular features extraction tool on 3D MRA using semiautomated open-curve active contour vessel tracing. Magn. Reson. Med. 79 (6), 3229–3238. https://doi.org/10.1002/mrm.26961.

Chen, Li, Hatsukami, Thomas, Hwang, Jenq Neng, Yuan, Chun, 2020. Automated intracranial artery labeling using a graph neural network and hierarchical refinement. ArXiv 1, 1–11.

Çiçek, Özgün, Abdulkadir, Ahmed, Lienkamp, Soeren S., Brox, Thomas, Ronneberger, Olaf, 2016. 3D U-Net: learning dense volumetric segmentation from sparse annotation. Lect. Notes Comput. Sci. (Incl. Subser. Lect. Notes Artif. Intell. Lect. Notes Bioinforma.) 9901 LNCS 424–432. https://doi.org/10.1007/978-3-319-46723-8_49.

Cohen, Jacob, 1960. A coefficient of agreement for nominal scales. Educ. Psychol. Meas. 20 (1), 37–46. https://doi.org/10.1177/001316446002000104.

Deshpande, Aditi, Nima Jamilpour, Bin Jiang, Patrik Michel, Ashraf Eskandari, Chelsea Kidwell, Max Wintermark, Laksari, Kaveh, 2021. Automatic segmentation, feature extraction and comparison of healthy and stroke cerebral vasculature. NeuroImage: Clin. 30 (March 2020), 102573 https://doi.org/10.1016/j.nicl.2021.102573.

Dice, Lee R., 1945. Measures of thE Amount of Ecologic Association between Species Author (s): Lee R. Dice published by: ecological society of america stable URL. Http://Www.Jstor.Org/Stable/1932409 Ecology 26 (3), 297–302.

Dunås, Tora, Anders Wåhlin, Khalid Ambarki, Laleh Zarrinkoob, Richard Birgander, Jan Malm, Anders Eklund, 2016. Automatic labeling of cerebral arteries in magnetic resonance angiography. Magn. Reson. Mater. Phys., Biol. Med. 29 (1), 39–47. https://doi.org/10.1007/s10334-015-0512-5.

Fan, Shengyu, Yueyan Bian, Hao Chen, Yan Kang, Qi. Yang, Tan, Tao, 2020. Unsupervised cerebrovascular segmentation of TOF-MRA images based on deep neural network and hidden markov random field model. Front. Neuroinformatics 13 (January), 1–10. https://doi.org/10.3389/fninf.2019.00077.

Fantazzini, Alice, Mario Esposito, Alice Finotello, Auricchio, Ferdinando, Pane, Bianca, Basso, Curzio, Spinella, Giovanni, Conti, Michele, 2020. 3D automatic segmentation of aortic computed tomography angiography combining multi-view 2D convolutional neural networks. Cardiovasc. Eng. Technol. 11 (5), 576–586. https://doi.org/10.1007/s13239-020-00481-z.

Fedorov, Andriy, Reinhard Beichel, Jayashree Kalpathy-Cramer, Julien Finet, Jean-Christophe Fillion-Robin, Sonia Pujol, Christian Bauer, et al., 2012. 3D slicer as an image computing platform for the quantitative imaging network. Magn. Reson. Imaging 30 (9), 1323–1341. https://doi.org/10.1016/j.mri.2012.05.001.

Flottmann, Fabian, Hannes Leischner, Gabriel Broocks, Jawed Nawabi, Martina Bernhardt, Tobias Djamsched Faizy, Milani Deb-Chatterji, Götz Thomalla, Jens Fiehler, Brekenfeld, Caspar, 2018. Recanalization rate per retrieval attempt in mechanical thrombectomy for acute ischemic stroke. Stroke 49 (10), 2523–2525. https://doi.org/10.1161/STROKEAHA.118.022737.

Fu, Fan, Jianyong Wei, Miao Zhang, Fan Yu, Yueting Xiao, Dongdong Rong, Yi. Shan, et al., 2020. Rapid vessel segmentation and reconstruction of head and neck angiograms using 3D convolutional neural network. Nat. Commun. 11 (1) https://doi.org/10.1038/s41467-020-18606-2.

Gao, Hongyang, Ji, Shuiwang, 2019. "Graph U-Nets." 36th International Conference on Machine Learning. *ICML 2019* 2019-June 3651–3660.

Gomez-Paz, Santiago, Akamatsu, Yosuke, Mallick, Akashleena, Jordan, Noah J., Salem, Mohamed M., Enriquez-Marulanda, Alejandro, Thomas, Ajith J., Ogilvy, Christopher S., Justin, M.Moore, 2021. Tortuosity index predicts early successful reperfusion and affects functional status after thrombectomy for stroke. World Neurosurg. 152, e1–e10. https://doi.org/10.1016/j.wneu.2021.02.123.

Goyal, Mayank, Bijoy, K.Menon, Zwam, Wim H.Van, Dippel, Diederik W.J., Mitchell, Peter J., Demchuk, Andrew M., Dávalos, Antoni, et al., 2016. Endovascular thrombectomy after large-vessel ischaemic stroke: a meta-analysis of individual patient data from five randomised trials. Lancet 387 (10029), 1723–1731. https://doi.org/10.1016/S0140-6736(16)00163-X.

Hadji, Sara El, Sara Moccia, Davide Scorza, Michele Rizzi, Francesco Cardinale, Giuseppe Baselli, Elena De Momi, 2019. Brain-vascular segmentation for SEEG planning via a 3D fully-convolutional neural network. Proc. Annu. Int. Conf. IEEE Eng. Med. Biol. Soc., EMBS 1014–1017. https://doi.org/10.1109/EMBC.2019.8857456.

Hatamizadeh, Ali, Tang, Yucheng, Nath, Vishwesh, Yang, Dong, Myronenko, Andriy, Landman, Bennett, Roth, Holger R., Xu, Daguang, 2022. UNETR: transformers for 3D medical image segmentation. Proc. - 2022 IEEE/CVF Winter Conf. Appl. Comput. Vis., WACV 2022, 1748–1758. https://doi.org/10.1109/WACV51458.2022.00181.

Hathout, Leith, Huy, M.Do, 2012. Vascular tortuosity: a mathematical modeling perspective. J. Physiol. Sci. 62 (2), 133–145. https://doi.org/10.1007/s12576-011-0191-6.

Holswilder, Ghislaine, Maaike, P.M.E.Stuart, Dompeling, Tine, Kruyt, Nyika D., Goeman, Jelle J., van der Lugt, Aad, Schonewille, Wouter J., et al., 2022. The prognostic value of extracranial vascular characteristics on procedural duration and revascularization success in endovascularly treated acute ischemic stroke patients. Eur. Stroke J. 7 (1), 48–56. https://doi.org/10.1177/23969873211067662.

Isensee, Fabian, Paul, F.Jaeger, Kohl, Simon A.A., Petersen, Jens, Klaus, H.Maier-Hein, 2021. NnU-Net: a self-configuring method for deep learning-based biomedical image segmentation. Nat. Methods 18 (2), 203–211. https://doi.org/10.1038/s41592-020-01008-z.

Jovin, Tudor G., Chamorro, Angel, Cobo, Erik, de Miquel, María A., Molina, Carlos A., Rovira, Alex, Luis San, Román, et al., 2015. Thrombectomy within 8 hours after symptom onset in ischemic stroke. N. Engl. J. Med. 372 (24), 2296–2306. https://doi.org/10.1056/nejmoa1503780.

Kaesmacher, J., Gralla, J., Mosimann, P.J., Zibold, F., Heldner, M.R., Piechowiak, E., Dobrocky, T., Arnold, M., Fischer, U., Mordasini, P., 2018. Reasons for reperfusion failures in stent-retriever-based thrombectomy: registry analysis and proposal of a classification system. Am. J. Neuroradiol. 39 (10), 1848–1853. https://doi.org/10.3174/ajnr.A5759.

Kaymaz, Z.O., Nikoubashman, O., Brockmann, M.A., Wiesmann, M., Brockmann, C., 2017. Influence of carotid tortuosity on internal carotid artery access time in the treatment of acute ischemic stroke. Interv. Neuroradiol. 23 (6), 583–588. https://doi.org/10.1177/1591019917729364.

Kliś, Kornelia, Roger Krzyżewski, Borys Kwinta, Krzysztof Stachura, Jerzy Gąsowski, 2019. Tortuosity of the internal carotid artery and its clinical significance in the development of aneurysms. J. Clin. Med. 8 (2), 237. https://doi.org/10.3390/jcm8020237.

Koo, Terry K., Mae, Y.Li, 2016. A guideline of selecting and reporting intraclass correlation coefficients for reliability research. J. Chiropr. Med. 15 (2), 155–163. https://doi.org/10.1016/j.jcm.2016.02.012.

Layton, Kennith, D. F, F., Kallmes, H.J., Cloft, E.P., Lindell, Cox, V.S., 2006. Bovine aortic arch variant in humans: clarification of a common misnomer. Am. J. Neuroradiol. 27 (7), 1541–1542.

Livne, Michelle, Jana Rieger, Orhun Utku Aydin, Abdel Aziz Taha, Ela Marie Akay, Tabea Kossen, Jan Sobesky, et al., 2019. "A U-Net Deep Learning Framework for High Performance Vessel Segmentation in Patients with Cerebrovascular Disease.". Front. Neurosci. 13 (FEB), 1–13. https://doi.org/10.3389/fnins.2019.00097.

Martin Bland, J., Altman, DouglasG., 1986. Statistical methods for assessing agreement between two methods of clinical measurement. Lancet 327 (8476), 307–310. https://doi.org/10.1016/S0140-6736(86)90837-8.

Mokin, Maxim, Muhammad Waqas, Felix Chin, Hamid Rai, Jillian Senko, Adam Sparks, Richard W.Ducharme, et al., 2020. Semi-automated measurement of vascular tortuosity and its implications for mechanical thrombectomy performance. Neuroradiology. https://doi.org/10.1007/s00234-020-02525-6.

Mont`Alverne, Francisco José Arruda, Fabricio Oliveira Lima, Felipe de Araújo Rocha, Diego de Almeida Bandeira, Adson Freitas de Lucena, Henrique Coelho Silva, Jin Soo Lee, Raul Gomes Nogueira, 2020. Unfavorable vascular anatomy during endovascular treatment of stroke: challenges and bailout strategies. J. Stroke 22 (2), 185–202. https://doi.org/10.5853/jos.2020.00227.

Nogueira, Raul G., Ashutosh, P.Jadhav, Haussen, Diogo C., Bonafe, Alain, Budzik, Ronald F., Bhuva, Parita, Yavagal, Dileep R., et al., 2018. Thrombectomy 6 to 24 hours after stroke with a mismatch between deficit and infarct. N. Engl. J. Med. 378 (1), 11–21. https://doi.org/10.1056/nejmoa1706442.

Penide, Joaquin, Mahmood Mirza, Ray Mc.Carthy, Jens Fiehler, Pasquale Mordasini, Patrick Delassus, Liam Morris, Gilvarry, Michael, 2021. Systematic review on endovascular access to intracranial arteries for mechanical thrombectomy in acute ischemic stroke. Clin. Neuroradiol. https://doi.org/10.1007/s00062-021-01100-7.

Phellan, Renzo, Alan Peixinho, Alexandre Falcão, Nils, D.Forkert, 2017. Vascular segmentation in TOF MRA images of the brain using a deep convolutional neural network. *Lect. Notes Comput. Sci. (Incl. Subser. Lect. Notes Artif. Intell. Lect. Notes Bioinforma.)* 10552 LNCS 39–46. https://doi.org/10.1007/978-3-319-67534-3_5.

Ribo, Marc, Alan Flores, Marta Rubiera, Jorge Pagola, Nuno Mendonca, David Rodriguez-Luna, Soco Piñeiro, Pilar Meler, Jose Alvarez-Sabin, Carlos, A.Molina, 2013. Difficult catheter access to the occluded vessel during endovascular treatment of acute ischemic stroke is associated with worse clinical outcome. J. NeuroInterventional Surg. 5 (SUPPL.1), 2–4. https://doi.org/10.1136/neurintsurg-2012-010438.

Ronneberger, Olaf, Philipp Fischer, Thomas Brox, 2015. U-net: convolutional networks for biomedical image segmentation. Lect. Notes Comput. Sci. (Incl. Subser. Lect. Notes Artif. Intell. Lect. Notes Bioinforma.) 9351, 234–241. https://doi.org/10.1007/978-3-319-24574-4_28.

Rosa, Joao Alves, Rachel Roberts, James Wareham, Robert Crossley, Anthony Cox, Alex Mortimer, 2021. Aortic and supra-aortic arterial tortuosity and access technique: impact on time to device deployment in stroke thrombectomy. Interv. Neuroradiol. 27 (3), 419–426. https://doi.org/10.1177/1591019920974183.

Schwaiger, B.J., Gersing, A.S., Zimmer, C., Prothmann, S., 2015. The curved MCA: influence of vessel anatomy on recanalization results of mechanical thrombectomy after acute ischemic stroke. Ajnr. Am. J. Neuroradiol. 36 (5), 971–976. https://doi.org/10.3174/ajnr.A4222.

Snelling, Brian, Samir Sur, M., Sumedh, S., Shah, Stephanie Chen, Simon, A., Menaker, David, McCarthy, J., Dileep, R., Yavagal, Eric, Peterson, C., Robert, M., Starke, 2018. Unfavorable Vascular Anatomy Is Associated with Increased Revascularization Time and Worse Outcome in Anterior Circulation Thrombectomy. In: World Neurosurgery, 120, pp. e976–e983. https://doi.org/10.1016/j.wneu.2018.08.207.

Tahoces, Pablo G., Santana-Cedrés, Daniel, Luis Alvarez, Miguel Alemán-Flores, Agustín Trujillo, Carmelo Cuenca, Jose, M.Carreira, 2020. Automatic detection of anatomical landmarks of the aorta in CTA images. Med. Biol. Eng. Comput. 58 (5), 903–919. https://doi.org/10.1007/s11517-019-02110-x.

Tang, Yucheng, Dong Yang, Wenqi Li, Holger Roth, Bennett Landman, Daguang Xu, Vishwesh Nath, and Ali Hatamizadeh. 2021. Self-Supervised Pre-Training of Swin Transformers for 3D Medical Image Analysis http://arxiv.org/abs/2111.14791.

Turk, Aquilla S., Siddiqui, Adnan, Fifi, Johanna T., Leacy, Reade A.De, Fiorella, David J., Gu, Eugene, Levy, Elad I., et al., 2019. Aspiration thrombectomy versus stent retriever thrombectomy as first-line approach for large vessel occlusion (COMPASS): a multicentre, randomised, open label, blinded outcome, non-inferiority trial. Lancet 393 (10175), 998–1008. https://doi.org/10.1016/S0140-6736(19)30297-1.

Yao, Linlin, Pengbo Jiang, Zhong Xue, Yiqiang Zhan, Dijia Wu, Lichi Zhang, Qian Wang, Feng Shi, Dinggang Shen, 2020. Graph convolutional network based point cloud for head and neck vessel labeling. *Lect. Notes Comput. Sci. (Incl. Subser. Lect. Notes Artif. Intell. Lect. Notes Bioinforma.)* 12436 LNCS 474–483. https://doi.org/10.1007/978-3-030-59861-7_48.

Yeo, Leonard L.L., Bhogal, Pervinder, Gopinathan, Anil, Cunli, Yang, Tan, Benjamin, Andersson, Tommy, 2019. Why does mechanical thrombectomy in large vessel occlusion sometimes fail?: a review of the literature. Clin. Neuroradiol. 29 (3), 401–414. https://doi.org/10.1007/s00062-019-00777-1.

Yoo, Albert J., Andersson, Tommy, 2017. Thrombectomy in acute ischemic stroke: challenges to procedural success. J. Stroke 19 (2), 121–130. https://doi.org/10.5853/jos.2017.00752.